JOURNAL OF GEOPHYSICAL RESEARCH, VOL. 90, NO. B6, PAGES 4537-4555, MAY 10, 1985

SOURCE PARAMETERS AND FAULTING PROCESSES OF THE 1959 HEBGEN LAKE, MONTANA, EARTHQUAKE SEQUENCE

Diane I. Doser[1]

Department of Geology and Geophysics, The University of Utah, Salt Lake City

Abstract. The August 1959 (M_S = 7.5) Hebgen Lake, Montana, earthquake is the largest earthquake to have occurred in the intermountain region in historic time. Studies of waveforms at regional and teleseismic distances indicate that the main shock of the sequence was a double event consisting of a shock of m_b = 6.3 (M_o = 3 x 10^{18} N m) followed 5 s later by one of m_b = 7.0 (M_o = 1 x 10^{20} N m). Comparisons between fault plane solutions from short-period first motion data, seismic moment tensors determined from the inversion of long-period body wave data, and observed surface faulting indicate that rupture occurred along one or more fault planes with strike orientations slightly discordant with the trace of surface faulting. A close association between the surface scarps and Laramide thrust faults also suggests that the events may represent normal faulting along reactivated older thrust faults. Focal mechanisms from short-period first motion data for aftershocks with $M_S > 5.5$ in northwestern Yellowstone National Park showed strike-slip, normal, and reverse mechanisms with a variety of nodal plane orientations that reflect the complex tectonics of the Yellowstone Plateau. Limited focal depth information suggests a decrease in the maximum focal depth of earthquakes from 15 km at Hebgen Lake to 6-10 km in northwestern Yellowstone National Park.

Introduction

Beginning August 18, 1959 a sequence of large ($6.0 \leq M_S \leq 7.5$) earthquakes occurred in the Hebgen Lake, Montana/northwestern Yellowstone National Park region along an east-west trending zone that defines a major junction in trends of the Intermountain seismic belt (Figure 1). This region is an area of complex tectonic interactions between the active Yellowstone Plateau volcano-tectonic system to the east and the mountainous terrain of southwestern Montana, consisting of Quaternary normal faults superimposed upon preexisting Laramide folds and thrusts [Smith and Sbar, 1974]. The main shock of the sequence (M_S = 7.5) represents the largest earthquake to have occurred in the intermountain region in historic time, and the study of the Hebgen Lake earthquake sequence provides new information on the nature of large normal fault earthquakes that are expected to occur in other parts of the region.

Although the 1959 Hebgen Lake sequence occurred before the establishment of the World-Wide Standard Seismograph Network, many stations were in operation at the the time of the earthquakes and provide a fairly complete data set at regional and teleseismic distances. Previous studies of the Hebgen Lake earthquakes [Ryall, 1962; Dewey et al., 1973] focused primarily on the determination of fault plane solutions for the larger events of the sequence and the relocation of epicenters. This study presents the first results of modeling of body waves as well as amplitude inversion for the seismic moment tensors of the main shock and several of the larger aftershocks. Results of the body wave modeling are compared with the patterns of surface faulting and geodetic information in an effort to reconstruct the faulting processes that occurred during the 1959 sequence. In addition, fault plane solutions are obtained for four other aftershocks. Data from this study and investigations by Dewey et al. [1973], Pitt et al. [1979], and Smith et al. [1977] are also used to examine tectonic processes in the Hebgen Lake-Yellowstone region.

Regional Geology and Tectonics

The Hebgen Lake-northern Yellowstone region lies in an area of complex geology where late Tertiary block faulting is superimposed on preexisting regional thrust faults and folds of Laramide age [Witkind et al., 1964]. These structures, in turn, are disrupted by more recent faulting and igneous activity associated with Quaternary development of the Snake River Plain-Yellowstone volcano-tectonic system [Smith and Christiansen, 1980].

Prominent faults in the region that show evidence of Quaternary movement are noted in Figure 2. The Madison fault, bounding the western edge of the Madison Range, has had an estimated 11 m of post-Pinedale (<15,000-30,000 years B.P.) movement [Mathieson, 1983]. A 1-m scarp was formed along a 3-km segment of the fault adjacent to Madison Canyon during the 1959 earthquake [Myers and Hamilton, 1964]; however, it is difficult to determine whether this movement was related to compaction of valley sediments or to tectonic movement along the fault.

The southern end of the Madison Range is broken by the Red Canyon and Hebgen faults (Figures 2 and 3) that were activated in the 1959 earthquake. Vertical displacements of up to 6.7 m [Myers and Hamilton, 1964] occurred along the Red Canyon fault during the 1959 main shock. The Red Canyon fault scarp borders the southern side of Kirkwood Ridge, a ridge produced by the differential erosion of an overturned limb of a Laramide fold (Figure 4) that forms an arc with a curvature of over 90°. The Red Canyon fault closely follows a contact between massive lime-

[1]Now at Seismological Laboratory, California Institute of Technology, Pasadena.

Paper number 4B5164.
0148-0227/85/0048-5164$05.00

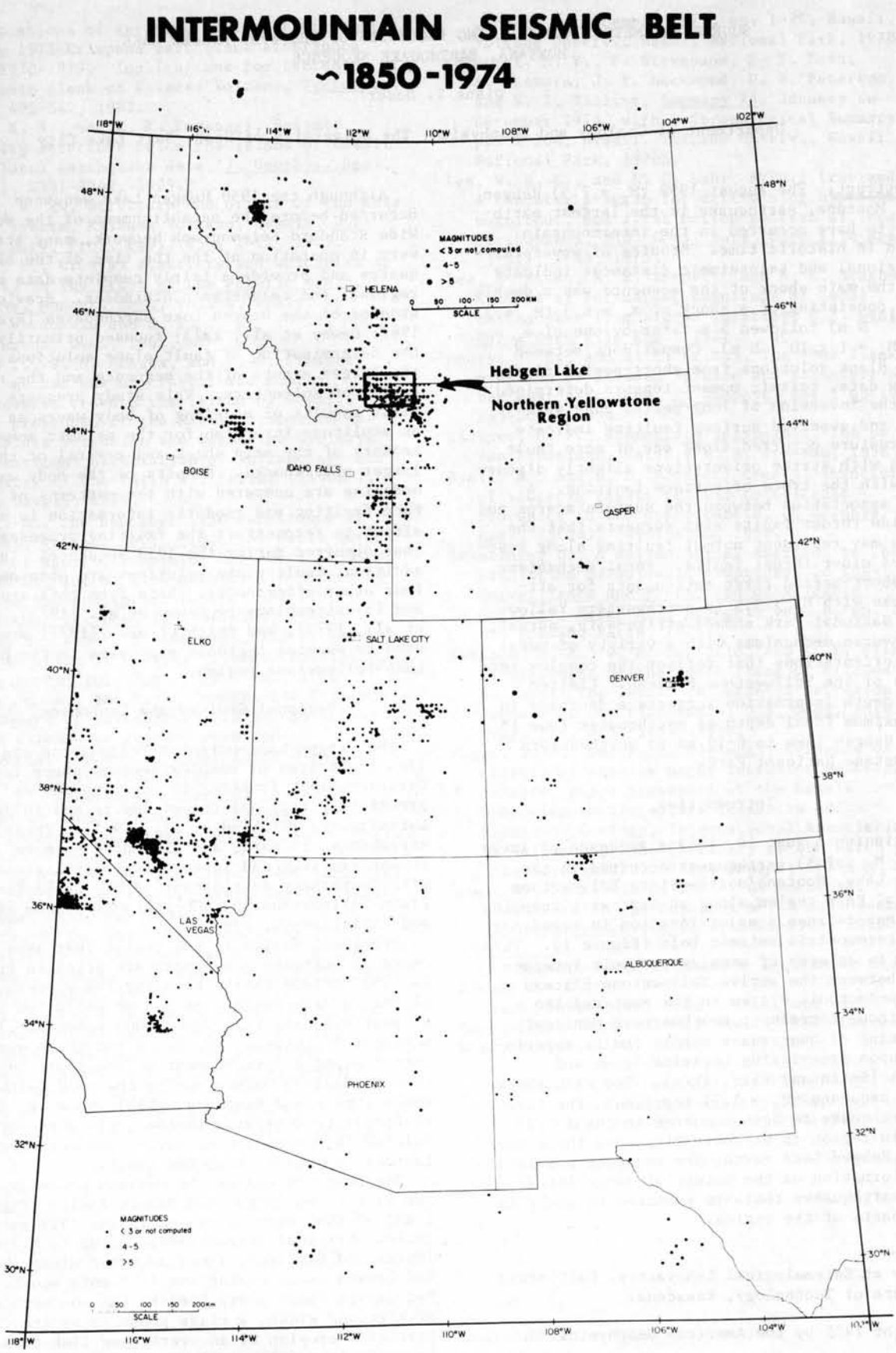

Fig. 1. Intermountain seismic belt (modified from Arabasz and Smith [1979]) with Hebgen Lake/northern Yellowstone study area. Seismicity is for the period 1850-1974.

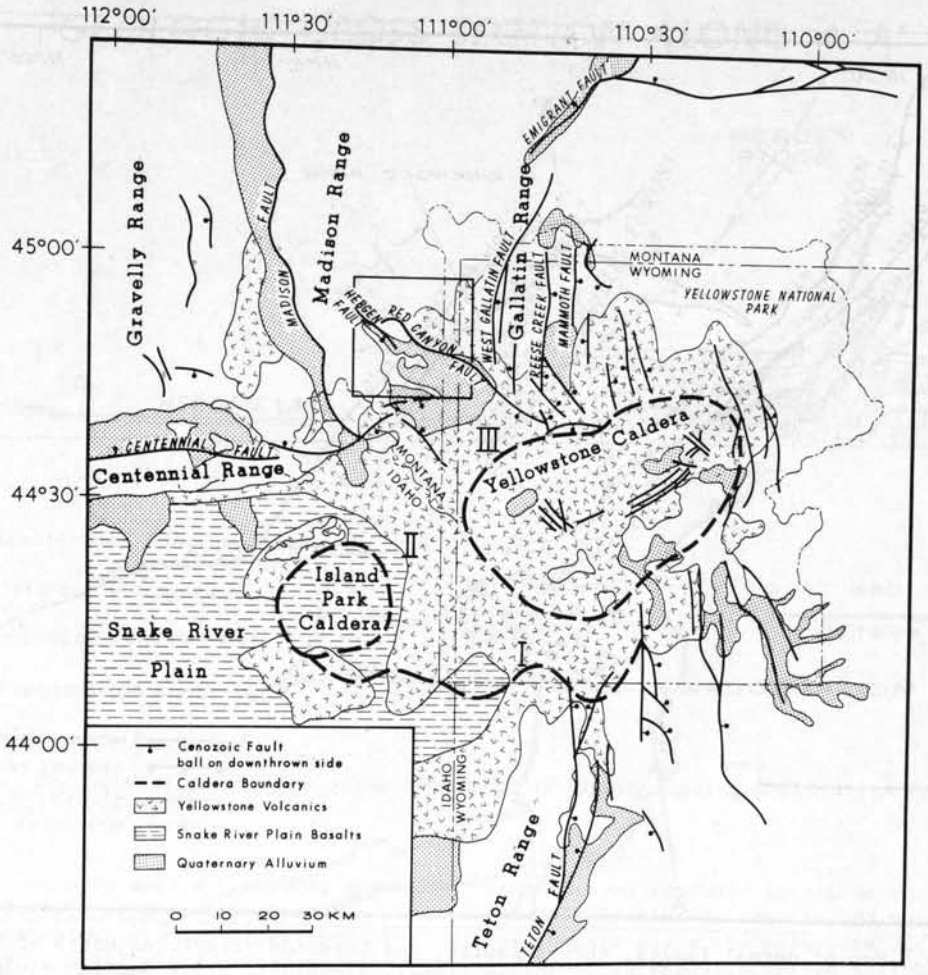

Fig. 2. Generalized geology of the Hebgen Lake region. Major Quaternary faults [Smith and Christiansen, 1980; U.S. Geological Survey, 1972] and mountain ranges are shown. Roman numerals refer to calderas sequentially produced during three cycles of volcanism in the Yellowstone area [Smith and Christiansen, 1980]. The boundary of the oldest caldera, I, is only partially recognized. The box outlines the area shown in Figure 3.

stone and thin bedded shale. Displacement on the fault has been down the dip of these beds [Myers and Hamilton, 1964]. On both ends of Kirkwood Ridge where the bedding planes revert to an upright attitude, the fault scarp dies away in a series of small fractures. The divide thrust fault flanks the northern edge of Kirkwood Ridge and parallels the Red Canyon fault for much of its length. The Hebgen fault scarp (Figures 3 and 4) also parallels a thrust fault for most of its length and is located about 300 m to the southwest of the thrust fault [Witkind et al., 1964]. The Hebgen fault forms the southwest edge of Hebgen Ridge (Figure 3) that is bounded to the north by the Wells thrust fault. Maximum vertical displacement after the 1959 earthquake along the Hebgen vault was 6.1 m [Witkind, 1964]. These observations suggest a possible association between the 1959 normal faulting and the Laramide thrust faults.

Other faults in the region that show evidence of postglacial movement include the Reese Creek and Mammoth faults in northwestern Yellowstone and the Centennial fault (Figure 2). The Centennial fault trends east-west at an angle of ~40° to the trend of the Snake River Plain-Yellowstone system, in contrast to the previously mentioned faults that follow the north to northwest structural grain of Laramide structures. Southeast of the Hebgen Lake region, the Teton fault trends at an angle of 40° to the Snake River Plain, cutting obliquely across older Laramide structures. This pattern suggests that the origin of the Centennial and Teton ranges may be related to the development and subsidence of the Snake River Plain.

Beginning 15 m. y. ago, volcanism of the Snake River Plain system began a systematic propagation northeastward from near the Boise, Idaho, area at a rate of 3-4 cm/yr [Armstrong et al., 1975]. As the rhyolitic volcanism progressed northeastward toward Yellowstone, a subsided region or downwarp, flooded by basalts, was left in its wake. This volcanic system trends at an acute angle across both Laramide and Tertiary structures and does not appear to be deformed along the trends of the older structures. Late Quaternary deformation of southwestern Montana has at least partly occurred in response to the subsidence of the Snake River Plain and the uplift of the Yellowstone Plateau, producing the youthful east-west

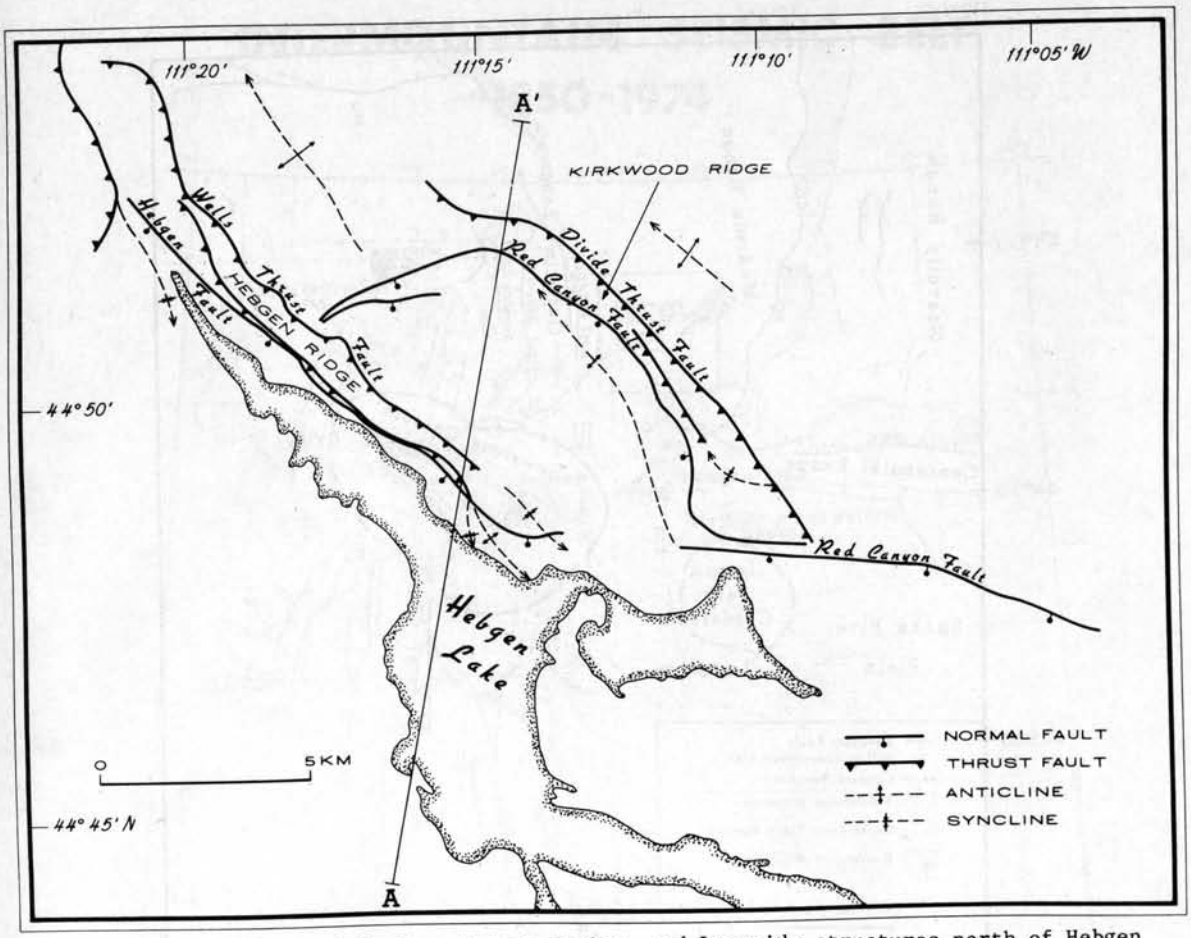

Fig. 3. Map of normal faults, thrust faults, and Laramide structures north of Hebgen Lake, adapted from U.S. Geological Survey [1964]. A geologic cross section along A-A' is shown in Figure 4.

trending Centennial fault zone and reactivating older faults that are favorably oriented with respect to the current stress field.

Historical Seismicity

Prior to the 1959 Hebgen Lake earthquake sequence, at least 77 earthquakes were felt in the Hebgen Lake-Yellowstone region [Qamar and Stickney, 1983]. Before 1961 only 11 seismograph stations were located within 1000 km of the region [Trimble, 1973]; therefore the majority of these early earthquakes do not have well-determined epicenters. The largest documented earthquake occurring prior to 1959 was the November 23, 1947, Virginia City, Montana, earthquake with a modified Mercalli intensity of VIII. This earthquake was located near the Madison fault.

On August 17, 1959, at 1137 P.M. MST (August 18, 0637 UT) the first of a series of major and damaging earthquakes occurred in the Hebgen Lake region. Many seismograms of the main shock of this sequence show a distinct arrival occurring 5-8 s after the first P arrival. Because the amplitude of this second phase is always larger than the first phase and the time difference between the phases is 1 s greater for stations north of the epicentral area, it is concluded that the second phase is actually the P arrival from another event rather than a pP phase. Ryall [1962] first noted the possible existence of these two events in his study of the main shock. Although he did not attempt to locate the second event, he shows seismograms illustrating the arrivals from the two events.

Epicenters for the two events (the asterisks in Figure 5) were relocated using a Herrin [1968] earth model and arrival times picked by the author. The epicenters for the events were located to the north of the southward dipping Red Canyon and Hebgen fault scarps. The epicenter determined for the first subevent by Ryall [1962] (the diamond in Figure 5) also is located to the north of the fault scarps. Since at least 1974 there has been considerable microearthquake activity south of the fault scarps [Trimble and Smith, 1975; Smith et al., 1977], with relatively few microearthquakes located north of the surface breakage. These data suggest that the two events of the main shock probably occurred south of the fault scarps and that their epicenters have a north to northeast bias. This epicenter bias may have been caused by using P wave arrivals from stations in the southwestern United States whose ray paths pass through the Basin and Range province, an area of low upper mantle P wave velocities or by using an improper local velocity model. The velocity structure of the Hebgen

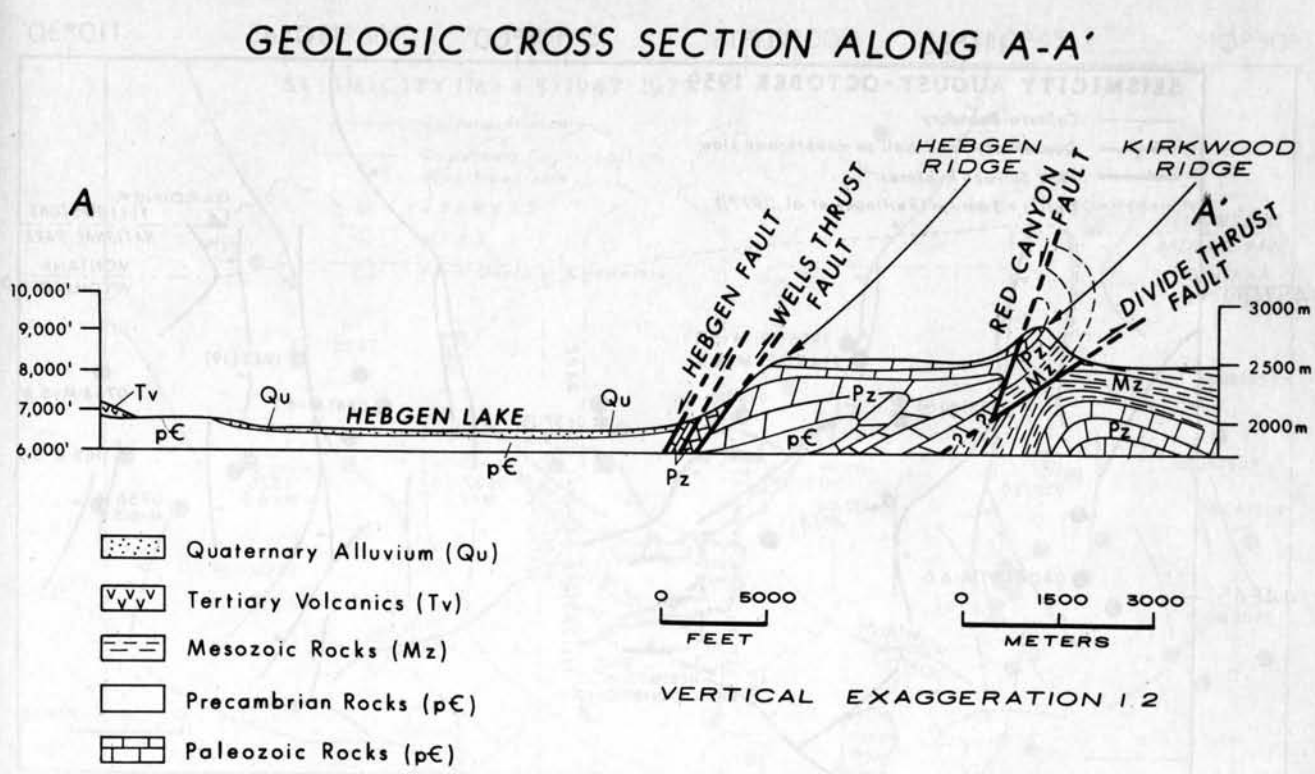

Fig. 4. Geologic cross section along line A-A' of Figure 3 using infomration from U.S. Geological Survey [1964].

Lake region has not been well determined; however, a detailed velocity model obtained for the northeastern Yellowstone Plateau from refraction data [Smith et al., 1982] shows P wave velocities to depths of 5 km that are 10-20% slower than the velocities of the Herrin [1968] model.

An attempt was made to eliminate some of these biases by relocating the 1959 events relative to the June 30, 1975 (M_L = 6.1), Yellowstone earthquake. Station delays at regional and teleseismic distances were determined by by fixing the epicenter of the 1975 earthquake at the location that Pitt et al. [1979] determined from local network data. These delays were then used to relocate the 1959 events. Unfortunately, many of the stations operating in 1959 were closed by 1975, and the azimuthal distribution of stations recording all three events was poor. The onset of the 1975 main shock at local and regional stations was emergent, suggesting that a foreshock of M4.5 preceded the main shock by 1 s [Pitt et al., 1979]. This also introduces error in the 1975 main shock location and station delays. The relocated epicenter for the first subevent (the square in Figure 5) is still north of the fault scarps, only 3 km south of the author's first relocation of the event. The station distribution for the second subevent was so poor that the relative relocation placed the event in central Idaho.

The apparent biases in all attempted relocations make it difficult to use the epicenter locations to determine the spatial relationship between the two events of the main shock and the observed ground breakage. One important observation that can be made is that the second event occurred 5-8 km to the south of the first event, since biases in their locations should be similar. It is also interesting to note that all relocations place the subevents near the southeastern end of observed surface wreckage.

Also shown in Figure 5 are the aftershock locations of the 1959 earthquake determined by Dewey et al. [1973] for the first 2 months following the main shock. Dewey et al. [1973] relocated these aftershocks using a joint epicenter method with Ryall's [1962] epicenter as the fixed event. Because Ryall's [1962] epicenter is also located northeast of the surface faulting, the aftershock locations may also have a northeast bias. In the first 24 hours of the sequence, five aftershocks with $M_S > 5.5$ occurred in northwestern Yellowstone National Park and are considered to be associated with an area of complex faulting near the edge of the Yellowstone caldera. On August 19 (UT) the activity shifted to 15 km west of the Madison Range with a M = 6.0 event. Aftershocks occurring later than August 19 were located within 10 km of earthquakes that occurred during the first 48 hours of the sequence, with the exception of one aftershock near the south shore of Hebgen Lake.

The aftershocks of the 1959 Hebgen Lake sequence define a broad region of seismicity 90 km long and 20 km wide striking nearly east-west. This trend does not align with the surface traces of any known Quaternary faults in the region except the Centennial fault. However, even when a possible northward bias of 10 km in the aftershock locations is taken into account, the aftershock epicenters are 10-15 km north of the Centennial fault.

Epicenters of earthquakes occurring between

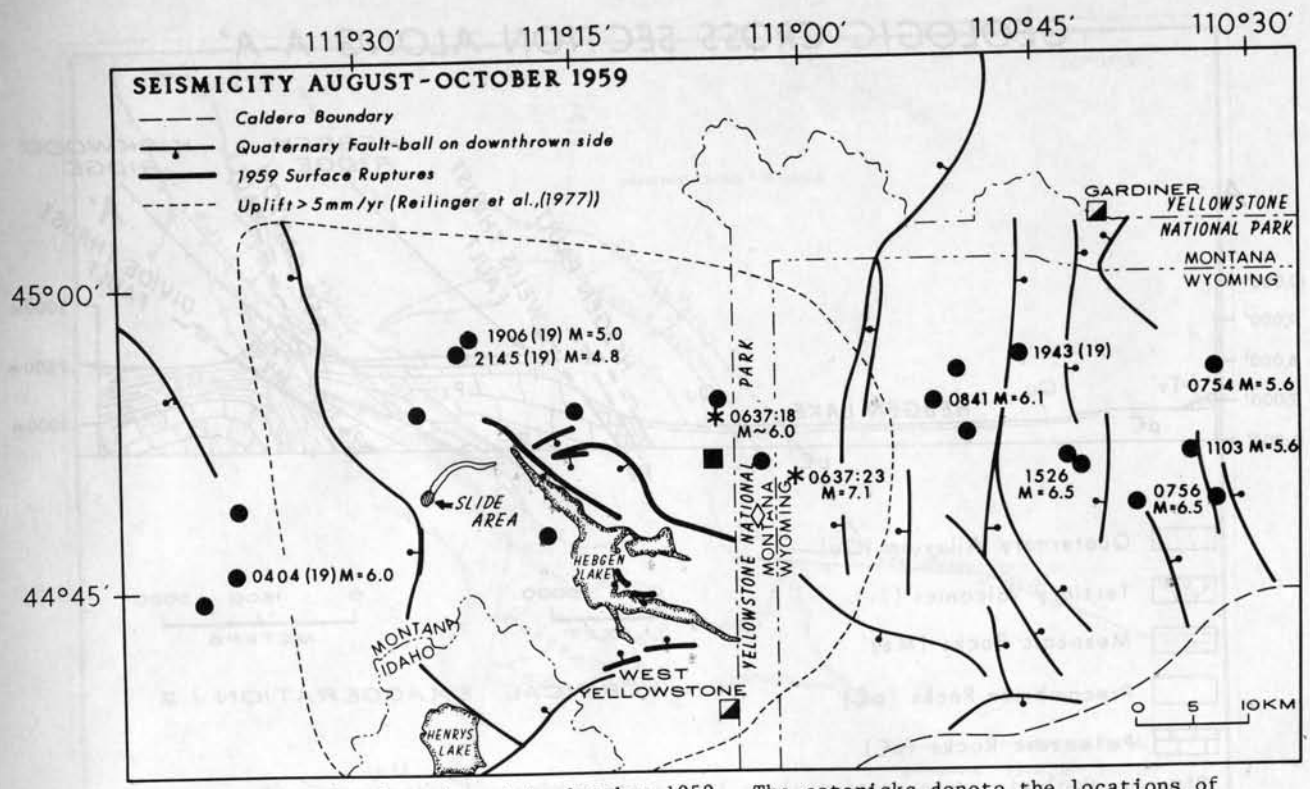

Fig. 5. Seismicity from August to October 1959. The asterisks denote the locations of the epicenters of the main shock subevents as determined by the author. The diamond shows the location of the first subevent as determined by Ryall [1962] using the method of least squares. The square is the location of the first subevent relative to the 1975 Yellowstone earthquake. Aftershocks locations are from Dewey et al. [1973]. Origin times and magnitudes (when available) are listed for earthquakes occurring on August 18 and 19 during the first 48 hours of the sequence. The "(19)" following some origin times denotes the earthquakes that occurred on August 19.

1947 and 1979 in the Hebgen Lake region (this study, Dewey et al. [1973], and Qamar and Stickney [1983]) with $M \geq 4.5$ are shown in Figure 6. Events with $M > 5.5$ include the October 21, 1964 ($m_b = 5.8$), earthquake located west of the Madison fault and the June 30, 1975 ($M_L = 6.1$), earthquake near the edge of the Yellowstone caldera at Norris Junction. Smith and Sbar [1974] consider the 1964 event to be an aftershock of the 1959 sequence. The east-west trend seen in seismicity during 1959 is not as apparent in these latter data; however, on a microearthquake level ($M<3.0$) the east-west trending zone is well defined [Smith et al., 1977; Smith and Christiansen, 1980]. Aftershocks of the 1975 earthquake broaden the zone to the east, extending southward into the Yellowstone caldera. A north-south trend of microearthquakes along the valley west of the Madison fault is also visible in the seismicity maps of Smith and Christiansen [1980]. The Hebgen Lake region south of the 1959 surface breakage has been very active at the microseismic level [Trimble and Smith, 1975], although no post-1959 $M>4.5$ earthquakes have occurred here. East of the August 18, 1959, aftershocks at 0756 and 1103 and the 1975 Norris Junction earthquake the east-west trend in seismicity is diffuse and extends eastward no more than 20 km.

The trend of the aftershock zone of the 1959 earthquake and post-1974 microearthquake activity suggests that seismicity in the region may be related to deformation taking place in the Snake River Plain-Yellowstone system. The length of the aftershock zone is comparable to that of the 1983 ($M_S = 7.2$) Borah Peak, Idaho, earthquake [Doser, 1984a], suggesting that aftershock zones with lengths of 75-100 km are not uncommon for normal fault earthquakes of $7.0 \leq M_S \leq 7.5$.

Reilinger et al. [1977], using pre-1959 regional geodetic data, have detected a broad zone of crustal doming in the Hebgen Lake area with relative uplift rates of up to 5 mm/yr (Figure 5). Much of the 1959 aftershock activity west of Yellowstone is located in this zone. Reilinger et al. suggest that intrusion of magma at a maximum point source depth of 20-35 km was responsible for the uplift but admitted that there was little geophysical evidence to support their hypothesis. We will evaluate this idea in light of additional seismic information in a later section.

Fault Plane Solutions

Fault plane solutions for the two events of the August 18 main shock and for six aftershocks that occurred within the first 24 hours of the sequence were determined from short-period first motion data using a Herrin [1968] velocity

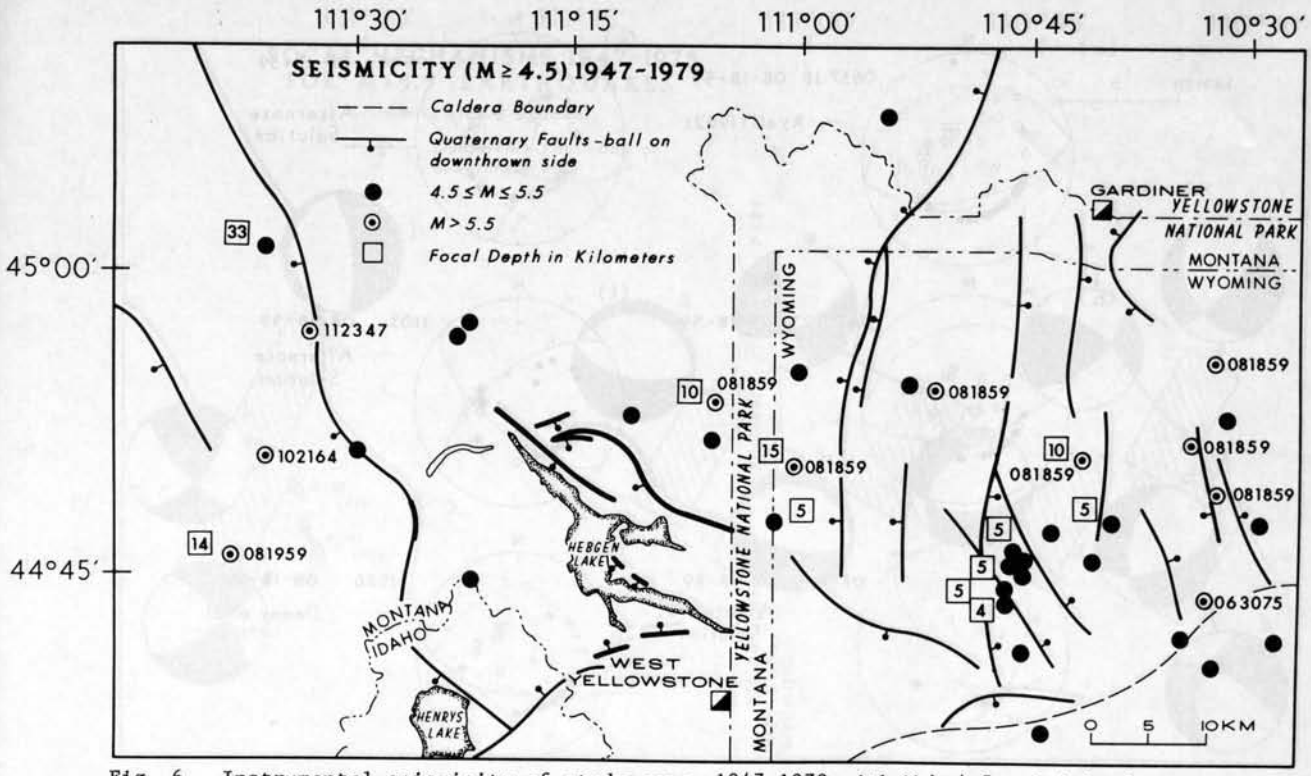

Fig. 6. Instrumental seismicity of study area, 1947-1979 with $M \geq 4.5$. Origin dates are indicated for earthquakes with $M > 5.5$.

model. Focal depths obtained from body wave modeling, as discussed in a later section, were used in the determination of fault plane solutions for the 0637 earthquakes and the aftershocks at 1526 and 0404. Focal depths for the remaining aftershocks were fixed at 12 km. Since only regional and teleseismic data were used in determining the focal mechanisms, the assumption of a fixed depth should not affect the takeoff angles by more than 3°-5°. Lower hemisphere projections of the fault plane solutions and first motion data are shown in Figure 7.

The two earthquakes at 0637:18 and 0637:23 had identical southward dipping nodal planes with a strike of $102^{\circ}\pm5^{\circ}$ and dip of $60^{\circ}\pm5^{\circ}$. This suggests that both events may have occurred along the same fault plane or along fault planes with similar orientation. The focal mechanism determined for the 0637:18 subevent is not significantly different than that determined by Ryall [1962] (strike = $100^{\circ}\pm10^{\circ}$; dip = $54^{\circ}\pm8^{\circ}$ SW) using a Jeffreys and Bullen [1940] velocity model. The good agreement between these solutions suggests that errors produced by using a improper local velocity model should not alter the nodal plane orientations by more than 5-10°.

The Hebgen Lake fault scarp and the eastern part of the Red Canyon scarp have an average trend of $130^{\circ}\pm10^{\circ}$, but the western part of the Red Canyon scarp has an arcuate shape. The southward dipping nodal planes determined for the two events of the main shock strike $102^{\circ}\pm5^{\circ}$. The average dip of the surface fault scarps is about $70^{\circ}\pm10^{\circ}$ S [Witkind, 1964] as compared to a dip of $60^{\circ}\pm5^{\circ}$ S for the nodal planes of the two events of the main shock. These results suggest that rupture at depth occurred along one or more fault planes that had dip orientations similar to the surface faulting but that had strike orientations that were slightly discordant with the surface faulting.

The axis of subsidence produced by the earthquakes in the West Yellowstone basin had a strike of 100° [Myers and Hamilton, 1964]. This strike is consistent with the trends of the nodal planes of the fault plane solutions. This suggests that subsidence in the basin was caused by movement at depth along the same fault or faults that generated the events at 0637:18 and 0637:23.

Focal mechanisms of earthquakes with $M_S > 5.5$ between 1947 and 1975 are shown in Figure 8. Solutions a-h were determined in this study. Because locations of the aftershocks are affected by the bias in the location of the first subevent, caution should be used in comparing these focal mechanisms with observed structure near their epicenters. The striped areas in Figure 8 indicate probable bias in the aftershock locations based on observed trends in microearthquake activity since 1975. In addition to these single event solutions, a number of surveys have determined composite fault plane solutions from microearthquakes in the region that are described in detail by Smith et al. [1977].

Several interesting nodal plane patterns are apparent in Figure 8. The region from the epicenter of the 1526 aftershock (solution g) westward to the Gravelly Range appears to be consistent with north-south extension (solutions a, b, h, and i), although Quaternary normal faults in the region predominantly strike northwest,

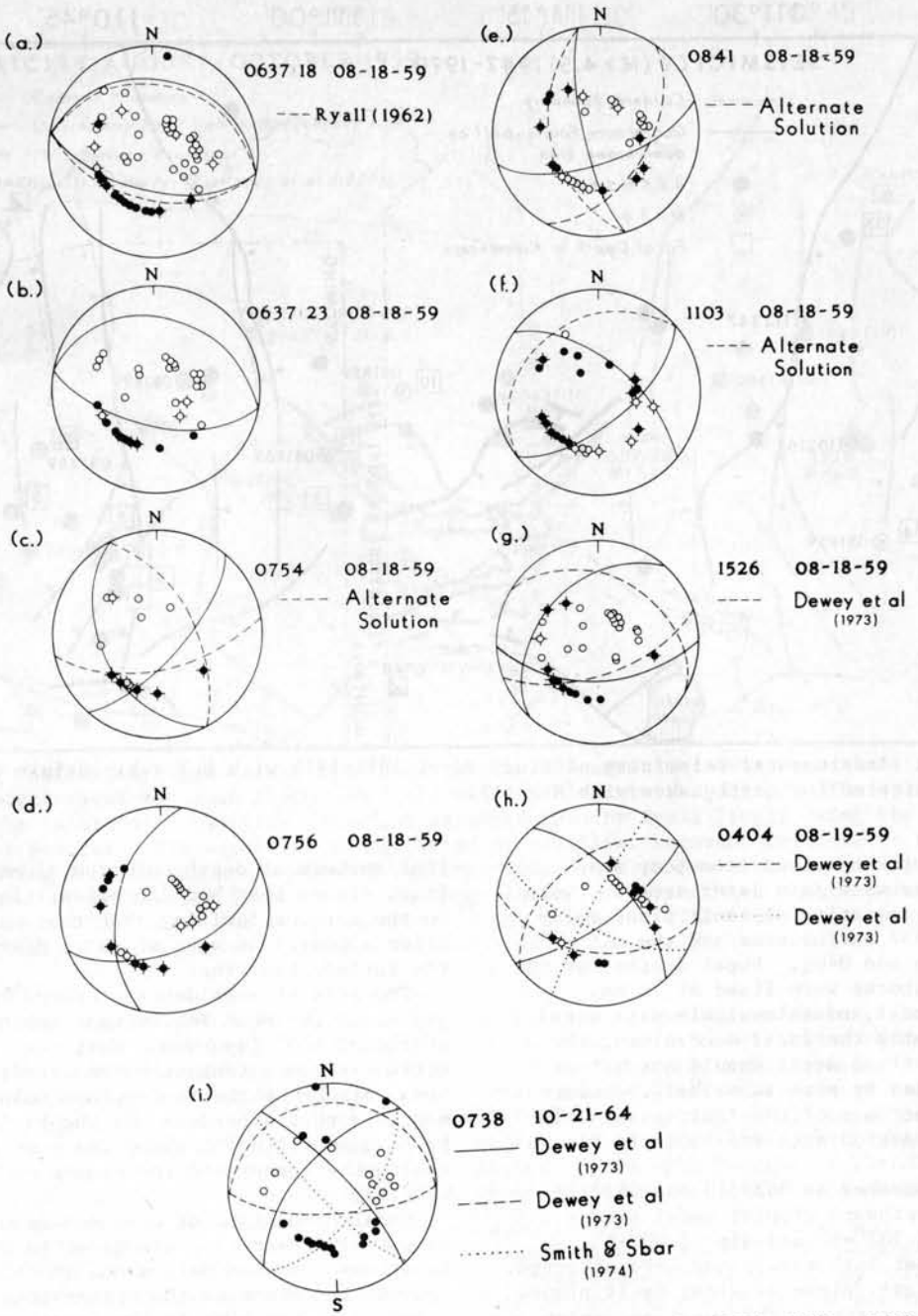

Fig. 7. Fault plane solutions for the 0637:18, 0637:23, 0754, 0756, 0841, 1103, 1526, and 0404 earthquakes. Projections are lower hemisphere, equal-area. Solid circles represent compressional first motions; open circles, dilatational first motions; crosses, near-nodal arrivals. Alternate solutions are shown by dashed lines.

paralleling Laramide structural trends. This suggests that earthquakes in the region may be occurring along reactivated older faults that are favorably oriented with respect to the present-day stress field. The character of faulting in this region of north-south extension also changes from dip slip to nearly strike slip in the west. Changes in focal mechanism with depth have been noted in the Great Basin [Vetter and Ryall, 1983]; however, the lack of good focal depth control for some of the Hebgen Lake epicenters makes it difficult to determine whether a similar process is taking place in this region.

Northwest of Hebgen Lake the focal mechanism for the November 23, 1947, earthquake (solution j) indicates east-west extension. This earthquake may have been a low stress drop event along the preexisting Madison fault zone, as suggested by Smith et al. [1977]. North and east of the 1526 aftershock (solution g) solutions d, e, and f show tension axes oriented east-west to northwest-southeast. Solution c is poorly constrained and should not be used in

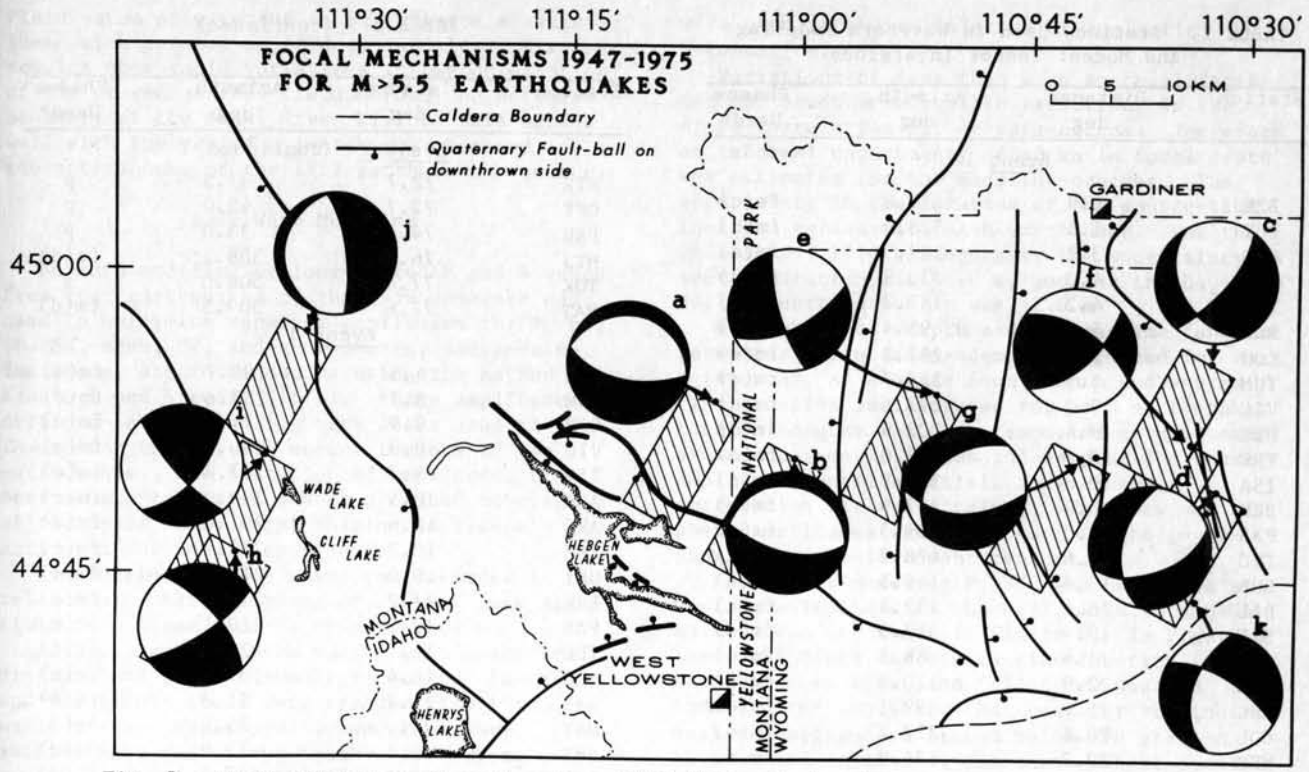

Fig. 8. Focal mehanisms of earthquakes, 1947-1975. Projections are lower hemisphere, equal-area. Open quadrants are dilataional; solid compressional. Focal mechanisms a-h are from this study (See Figure 7 and 8). Mechanism i (October 21, 1964) is from Smith and Sbar [1974], mechanism j (November 23, 1947) from Dewey et al. [1973], and mechanism k (June 30, 1975) from Bache et al. [1980]. The striped areas indicate probably bias in earthquake locations.

determining regional or local stress variations.

A mixture of normal, strike-slip, and oblique faulting was observed for the aftershocks of the 1975 (M_L = 6.0) Pocatello Valley (Idaho-Utah border) [Arabasz et al., 1981] and the 1983 Borah Peak, Idaho (M_S = 7.2) [Doser, 1984b], normal fault earthquakes. This suggests that it may not be uncommon to observe diverse patterns of faulting in the aftershocks of moderate to large normal fault earthquakes in the intermountain area.

The Norris Junction earthquake (solution k) and its aftershocks reflect minimum horizontal compressive stress axes oriented northeast-southwest [Pitt et al., 1979], whereas the orientation for solution d (M_S = 6.5), 10 km to the north, is northwest-southeast. This is suggestive of rapidly varying stress orientations near the caldera boundary. Sixty kilometers to the southeast of Hebgen Lake, east-west oriented tension axes are observed in the southern Yellowstone Plateau [Doser and Smith, 1983], implying that the least compressive stress direction rotates through 90° across Yellowstone, a feature earlier noted by Smith et al. [1977].

Furlong [1979] has modeled the Snake River

TABLE 1. Description of Earthquakes Used in This Paper

Event	Time UT	Date	Location	m_b	M_S	M_L	Focal Depth, km	M_o, x 10^{18} N m		Δσ, MPa
								Body Wave	Surface Wave	
1	0637:18.7	Aug. 18, 1959	44°52.80'N, 111°06.78'W	6.3			10	2.8		1.8
2	0637:23.8	Aug. 18, 1959	44°50.28'N, 111°01.56'W	7.0			15	9.2		9.7
3	1526:07.3	Aug. 18, 1959	44°51.0'N 110°43.2'W	6.5	6.3	6.7	10	3.1	5.5	1.7
4	0404:03.4	Aug. 19, 1959	44°45.6'N, 111°37.2'W	5.8	5.9	6.1	14	1.4	4.8	0.4

TABLE 2. Stations Used in Waveform Modeling and Moment Tensor Inversions

Station	Distance, deg	Azimuth, deg	Phases Used*
	Event 1		
BZE	0.9	7.8	fm(c)
BUT	1.5	318.3	fm(d)
LOG	3.2	189.5	fm(c)
HHM	4.0	330.9	fm(d)
SLC	4.2	187.7	fm(c)
RCD	5.7	95.4	fm(d)
LON	7.7	287.8	fm(d)
TUM	8.5	288.7	fm(d)
VIC	9.2	297.6	fm(d)
HBC	9.4	302.8	fm(d)
FRE	10.4	222.0	fm(c)
ISA	10.8	213.9	fm(c)
BRK	10.9	233.9	fm(c)
PAS	12.0	209.3	fm(c)
TUC	12.6	178.7	fm(c)
LUB	13.4	144.5	fm(c)
DAL	16.4	132.4	fm(c)
SIT	19.4	317.5	fm(d)
CLE	21.8	88.5	fm(d)
SHA	22.9	120.3	fm(d)
CHC	25.9	99.1	fm(d)
COL	28.4	327.7	fm(d)
MER	29.7	136.3	fm(d)
BEC	37.9	92.9	fm(d)
UWE	44.5	249.9	p
CAR	51.0	118.2	fm(d)
KIR	61.8	18.8	p
DBN	68.9	36.3	p
COP	69.1	30.4	p
UCC	69.5	37.7	p
LPZ	72.5	136.7	p
STR	72.7	37.5	p
CFF	72.7	42.0	p
PRU	74.4	33.0	p
MAT	77.6	309.5	fm(d)
	Event 2		
SEA	8.3	294.8	fm(d)
TUM	8.5	288.9	fm(d)
ARC	10.3	252.0	fm(c)
ALB	10.4	300.2	fm(d)
FRE	10.4	22.3	fm(c)
ISA	10.8	214.1	fm(c)
BRK	10.9	234.2	fm(c)
RVR	11.9	206.3	fm(c)
PAS	12.0	209.5	fm(c)
PLM	12.3	203.3	fm(c)
TUC	12.5	178.8	fm(c)
LUB	13.3	144.5	fm(c)
DAL	16.3	132.3	fm(c)
OTT	24.8	76.1	fm(d)
MNT	26.3	75.2	fm(d)
PAL	27.3	84.9	fm(d)
UWE	44.5	249.9	fm(d)
CAR	51.0	188.2	fm(d)
DBN	69.0	36.3	p,s
COP	69.1	30.4	p,s
UCC	69.6	37.7	p
LPZ	72.5	136.7	p

TABLE 2. (continued)

Station	Distance, deg	Azimuth, deg	Phases Used*
	Event 2 (continued)		
STR	72.7	37.5	p
CFF	72.7	42.0	p
PRU	74.4	33.0	p
MTJ	76.8	308.2	fm(d)
TOK	77.4	308.0	s
MAT	77.6	309.5	fm(d)
	Event 3		
SLC	4.3	190.7	fm(d)
TUM	8.7	287.6	fm(d)
COR	8.9	271.6	fm(d)
VIC	9.3	296.5	fm(c)
TIN	9.7	217.8	fm(c)
ALB	10.5	299.0	fm(c)
ARC	10.6	251.6	fm(d)
FRE	10.7	222.7	fm(c)
UKI	10.9	241.8	fm(d)
BRK	11.2	234.3	fm(c)
PAS	12.3	210.1	fm(c)
TUC	12.7	179.9	fm(c)
FLO	16.4	105.1	fm(c)
WAS	25.7	91.8	fm(d)
MNT	26.0	75.6	fm(d)
SHF	26.4	73.0	fm(d)
COL	28.5	327.4	fm(d)
HAL	33.1	73.5	fm(d),s
HON	45.3	254.5	fm,d
KIR	61.6	18.9	p,s
HUA	65.2	141.3	s
UPP	67.3	25.4	p
DBN	68.7	36.5	p,s
COP	68.8	30.5	p
UCC	69.3	37.9	p
STR	72.4	37.7	p
LPZ	72.5	137.0	p
STU	72.9	36.8	p,s
PRU	74.1	33.2	s
MTJ	76.9	308.3	p,s
MAT	77.7	309.7	p,s
SUV	89.8	243.9	p
	Event 4		
LOG	2.9	184.4	fm(c)
PAS	11.7	208.4	fm(c)
FAY	15.3	118.3	fm(c)
MNT	26.6	74.6	fm(c)
SHF	27.0	72.1	fm(c)
PAL	27.7	84.2	fm(d),s
SFA	28.2	70.4	fm(c)
RES	31.0	8.5	s
HAL	33.7	72.7	s
UPP	67.8	25.0	fm(d),s
STR	73.0	37.3	fm(d)
CLL	73.1	32.7	fm(d)
STU	73.5	36.4	fm(d)
TOL	73.6	49.9	fm(d)
MAT	77.5	309.3	fm(d)

**Phases are fm, first motion; d, dilatation, c, compression; p, p wave; s, s wave.

Plain as an arcuate cut in an infinite elastic sheet with tension applied at infinity. His results show rapid variations in the orientation of the present stress field across the northern boundary of the Snake River Plain. This agrees well with the varied orientations observed in the aftershocks of the 1959 earthquake sequence.

Body Wave Modeling

Forward modeling of long-period P and S waves from four earthquakes of the 1959 sequence was used to determine receiver amplitudes for P, pP, sP, SH, shSH, SV, and svSV phases, source-time functions, and focal depths using the method of Kanamori and Stewart [1976]. Phase amplitudes obtained in the modeling were later used to invert for the seismic moment tensors of the earthquakes. The inclusion of amplitudes from near-source reflected phases provided coverage of the upper hemisphere, helping to reduce errors in the inversion process.

Long-period S and P waveforms recorded in the teleseismic distance range of 25°-90° were digitized from paper records at a rate of 4 samples/s. Sample length varied with epicentral distance and the instrument response. The mean and the linear trend were removed from the waveforms and horizontal seismograms were rotated into radial and transverse components.

Kanamori and Stewart [1976] modeled long-period seismograms in a simple way by superimposing wavelets that have the same trapezoidal source-time function but are delayed with respect to one another by times corresponding to a given focal depth. This signal is then convolved with an instrumental response function and a causal Q operator to obtain the final synthetic.

The modeling procedure for each seismogram consisted of several steps. First estimates of the focal depth, the amplitude polarities, and the duration of faulting were made. These estimates were used to generate the initial synthetic for comparison with the observed data. Then the focal depth was varied in 1-km intervals from a point 10 km below the initial depth estimate to a point 10 km above the initial estimate. Next the source-time function length was varied in 0.2-s intervals from a value 2 s longer than the initial estimate to a value 2 s shorter than the initial estimate. Once the general waveform shape had been satisfactorily modeled the amplitudes of the direct and reflected phases were varied to obtain the best fit between the data and the synthetic. Goodness of fit was determined by examining the cross correlation of the data with synthetic. Stations used in the modeling process are listed in Tables 1 and 2.

The sS-S, pP-P, and sP-P delay times used in generating the synthetic were obtained from the Jeffreys and Bullen [1940] tables. The tables were interpolated to a focal depth interval of 1 km and an arc distance of 1°. The maximum accurately determined focal depth for microearthquakes in the Hebgen Lake-Yellowstone region is about 15 km [Smith et al., 1977]; the tables were thus interpolated to a depth of 25 km. Attenuation factor t^* values of 1.0 for P waves and 4.0 for S waves [Kanamori and Stewart, 1976] were used in the calculation of anelastic attenuation.

Variations of less than 2 km in focal depth did not produce noticeable variations in the cross-correlation fit of seismograms. Therefore an informal uncertainty of ± 2 km in focal depth was estimated for the modeling process. The uncertainty in the duration of the source-time function varies with each earthquake. For the 0637:18 and 1526 earthquakes, the uncertainty in source duration was ± 1.0 s, and for the 0404 and 0637:23 earthquakes it was ± 2.0 s.

Once the focal depth and source-time function parameters were independently estimated for each seismogram, an average focal depth and source-time function was computed for each earthquake. Each seismogram was then remodeled using these average parameter values and varying the phase amplitudes until a satisfactory cross-correlation fit was obtained. This new set of phase amplitudes was later used in the inversions for seismic moment tensors.

Results of modeling P, SV, and SH phases at various azimuths from the 0637, 1526, and 0404 earthquakes are shown in Figure 9. In Figure 9 the focal depth and source-time function (rise time, plateau time, and fall time) used in modeling the synthetic that best fit the individual seismogram are listed below the station azimuth and epicentral distance. Where possible the P waves of the 0637 earthquakes were modeled simultaneously; however, in a few cases the P waves of the 0637:23 event had been clipped or faintly recorded and only the first event could be modeled. The arrows in Figure 9 indicate the P wave arrivals of the two earthquakes. Average source parameters for the earthquakes are listed in Table 3.

Focal depths obtained from the modeling indicated that the 0637:18 event occurred at a depth of 10 ± 2 km and the 0637:23 event at a depth of 15 ± 3 km. Studies of maximum depths of microearthquakes in the Hebgen Lake region indicate that the base of the seismogenic zone is located at about 15 km [Smith et al., 1977], suggesting that the 0637:23 event, the largest earthquake of the sequence, occurred at or near the base of the seismogenic zone. These focal depths suggest that if a magma body exists in the crust, as suggested by Reilinger et al. [1977], it must be located at depths greater than 15 to 20 km.

Sibson [1982] has observed that many large ($M > 5.5$) earthquakes tend to nucleate near the base of the seismogenic zone and has postulated that this region has the highest concentration of strain energy and shear resistance. The direction of rupture for these large earthquakes appears to be upward from the base of the seismogenic zone, suggesting that the 0637:23 event may have ruptured upward to produce the observed surface scarps.

Smith and Bruhn [1984] have calculated the depths to the frictional/quasi-plastic transition zone for different crustal rheologies and thermal regimes for strain rates from 10^{-11} to 10^{-16} s^{-1}. Although no heat flow values have been measured in the immediate vicinity of Hebgen Lake, heat flow measured 20-30 km north and northeast of Hebgen Lake (outside of the national park boundaries) is 80-85 mW/m^2 (D. D.

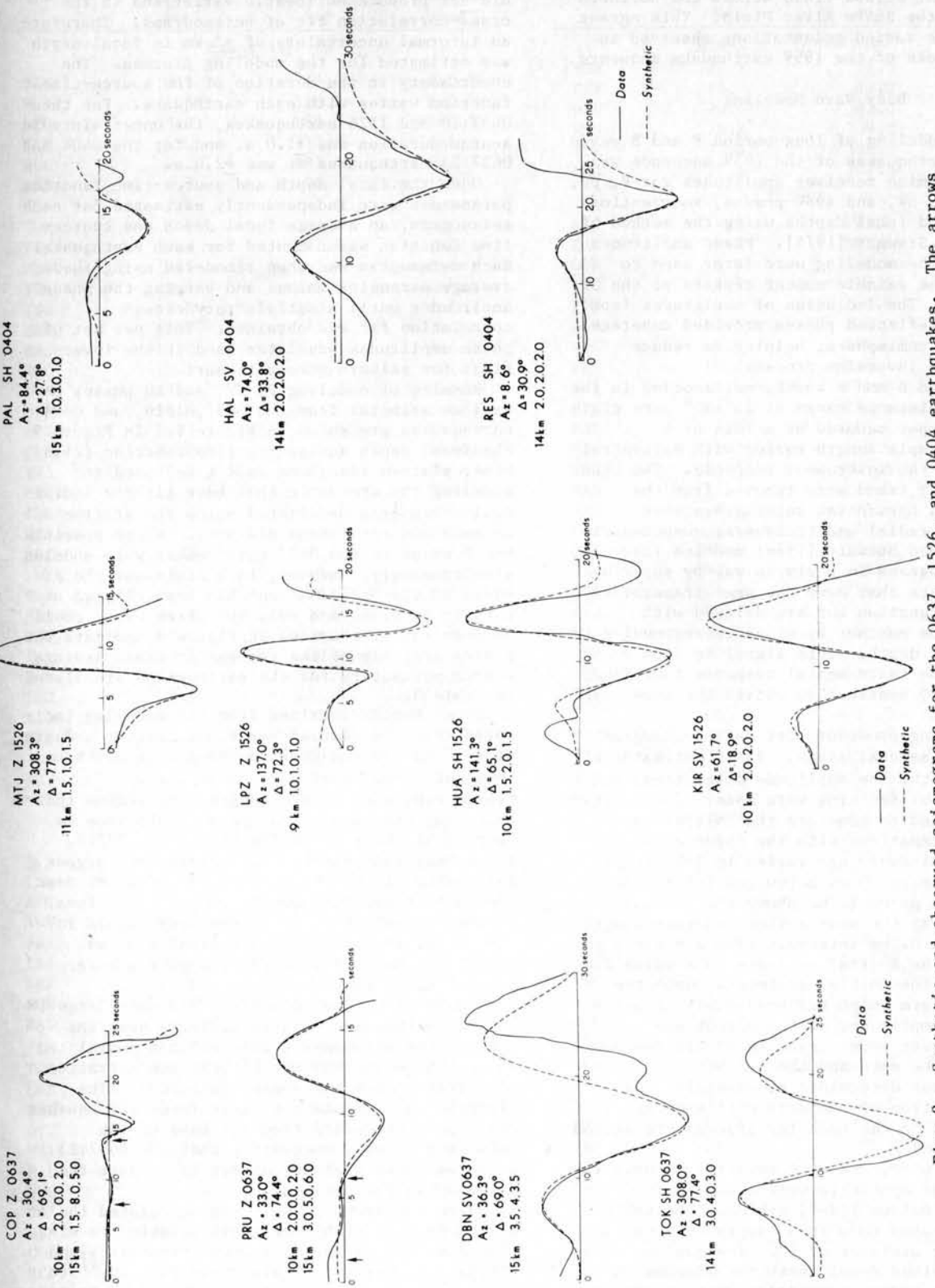

Fig. 9. Synthetic and observed seismograms for the 0637, 1526, and 0404 earthquakes. The arrows denote the P arrivals of the subevents of the main shock. The focal depths and source-time functions that best fit the individual seismograms are listed below the station azimuths (Az) and epicentral distances (Δ). The seismograms at PRU, DBN, LPZ, and KIR were recorded by Galitizins with T_s=7 to 25 s and T_g=7 to 25 s. Seismograms at MTJ, HUA, and HAL were recorded by Columbias with T_s=15 s and T_g=7 to 75 s. Sprengnethers with T_s=15 to 20 s and T_g=20 to 115 s recorded the seismograms at HAL and RES. A mainka with T_s=10 and a Wiechert with T_s=6 recorded the seismograms at TOK and COP, respectively.

TABLE 3. Source Parameters From Body Wave Modeling

Earthquake	Magnitude m_b	Number of Seismograms Modeled	Focal Depth km	Source-Time Functions, s		
				Rise	Plateau	Fall
0637:18	6.3	9	10	2	0	2
0637:23	7.0	10	15	3	4	3
1526:00	6.5	23	10	2	1	2
0404:00	5.8	6	14	2	2	2

Earthquake	Scalar Double-Couple Moment*	Fault width, km	Unilateral Rupture Length, km	Average Displacement, m	Stress Drop, M Pa
0637:18	2.8	14.9	6	1.0	1.8
0637:23	92.0	19.6	21	6.6	9.7
1526:00	3.1	13.0	9	0.5	1.7
0404:00	1.4	15.8	12	0.2	0.4

*Mutiply by 1×10^{18} for N m.

Blackwell, unpublished data, 1980). If we assume a strain rate of 10^{-14} to 10^{-15} s^{-1}, values characteristic of regional deformation in orogenic belts [Pfiffner and Ramsay, 1982], and the 90 mW/m^2 heat flow model of Smith and Bruhn [1984], the depth to the brittle-ductile transition can be estimated. For diabase, a probable constituent of lower crustal rocks, Smith and Bruhn's model predicts a transition depth of 16-18 km, again suggesting that the 0637:23 event occurred at or near the base of the seismogenic zone.

Smith et al. [1977] observed that the maximum focal depths of microearthquakes appear to decrease from Hebgen Lake southeastward toward the Yellowstone caldera. Focal depths to the south and southeast of the 1526 earthquake are even shallower (Figure 6), with aftershocks of the 1975 earthquake reaching a maximum depth of 6 km [Pitt et al., 1979]. Smith et al. [1977] estimated an average Curie depth of 10 ± 3 km from magnetic data for anomalies outside the caldera. The geotherm that obtains a Curie temperature at this depth is characteristic of a surface heat flow of 115 mW/m^2 [Smith et al., 1977]. Using Smith and Bruhn's [1984] 120 mW/m^2 model and a strain rate of 10^{-14} to 10^{-15} s^{-1}, the depth to the brittle ductile transition for diabase is 12-14 km, suggesting that the 1526 (M_S = 6.3) aftershock with a focal depth of 10 ± 2 km also may have occurred at or near the base of the seismogenic zone.

Body Wave Amplitude Inversion

Amplitudes obtained from the waveform-modeling process described in the preceding section were used to invert for an unconstrained seismic moment tensor and a moment tensor constrained to a double couple. When the minimization of the L1 norm, a summation of absolute values of residuals, is used as the optimum solution criterion in the inversion, first motion polarities can be included in the data set to help constrain the solution. Use of this minimization as the solution criterion is also more robust than minimization of the sum of squared residuals, the L2 norm [Claerbout and Muir, 1973]. The L1 norm inversions in this study are based on routines developed by Fitch et al. [1980]. The method of Strelitz [1978] was used to impose constraints in the inversion for the constrained moment tensor.

Because standard errors for the moment tensor components cannot be estimated using the formulation of Fitch et al. [1980], a series of test inversions were run on synthetic amplitude data for a pure double-couple source to determine how well the inversion process could resolve the source when noise in the data or errors in other parameters were introduced. Crustal velocities, station distributions, polarities and magnitudes of amplitude data, and hypocenter location were varied from the original data set, and solutions obtained from these perturbed values were compared to the results of the original inversion. Although the percentage of double couple in the unconstrained moment tensor often changed markedly by varying the data set, the orientation of the double couple component appeared to be very stable and usually varied less than 5° from the original source orientation. Therefore an informal uncertainty of $\pm5^\circ$ was estimated for the strike and dip of the nodal planes obtained in the inversion process.

Amplitudes of phases that were obtained in the modeling process (described in the preceding section) must be reduced to the focal sphere before being inverted. First, amplitudes were normalized to a distance of 60° using the amplitude-distance functions of Sengupta [1975] and the geometrical spreading correction of Bullen [1963]. The amplitudes were then corrected for free surface effects at the receiver and near the source, if appropriate, using corrections discussed by Bullen [1963] and Ewing et al. [1957]. The near-source and near-receiver structures were approximated by elastic half spaces. Focal depths used in the inversion were obtained from body wave modeling (Table 3). A Herrin [1968] earth model was used to obtain hypocentral P wave velocities. The receiver crustal velocity was set at 5 km/s. First motion polarities used in the inversion were read from long-period instruments. Moment tensors obtained in the inversion are listed in Table 4.

The unconstrained moment tensors for the

TABLE 4a. L1 Unconstrained Moment Tensor Solutions

Event	Mnn*	Mne	Mee	Mnz	Mez	Mzz
0637:18	1.78	0.560	0.280	0.136	0.464	-1.352
0637:23	14.7	10.9	0.000	-2.94	9.66	18.48
1526:00	1.146	-0.111	0.000	-0.205	-0.066	1.368

Event	Res†	%M	%DC	%CLVD
0637:18	0.17	12	84	4
0637:23	0.15	5	88	7
1526:00	0.17	5	85	10
0404:00	0.14	23	50	26

*Multiply by 1 x 10^{18} for N m.
†Absolute average residual, pertains to amplitude data only %M, %DC, %CLVD=percent monopole, dipole, and compensated linear vector dipole.

0637:18 and 0637:23 earthquakes are 84-88% double couple. The orientation of the double-couple component of the unconstrained moment tensor for the 0637:18 earthquake is the same as the orientation of the constrained moment tensor (Figure 10). Both solutions have a nodal plane that dips $42^{\circ}\pm5^{\circ}$ S with a strike of $95^{\circ}\pm5^{\circ}$. The unconstrained solution for the 0637:23 earthquake has one nodal plane with a strike of $93^{\circ}\pm5^{\circ}$ and dip of $48^{\circ}\pm5^{\circ}$ S, while the constrained solution has a southward dipping nodal plane with a strike of $86^{\circ}\pm5^{\circ}$ and a dip of $52^{\circ}\pm5^{\circ}$. These data again suggest that the two events occurred along the same fault plane or along fault planes with similar orientation.

The unconstrained moment tensor for the 1526 earthquake is 85% double couple, and its double-couple component has a nodal plane with a strike of $83^{\circ}\pm5^{\circ}$ and dip of $50^{\circ}\pm5^{\circ}$ S. This is nearly identical to the orientation of the constrained tensor that has a nodal plane with a strike of $85^{\circ}\pm5^{\circ}$ and dip of $57^{\circ}\pm5^{\circ}$ S. (Figure 10). These nodal planes agree well with the southward dipping nodal plane obtained from short-period first motion data with a strike of $89^{\circ}\pm10^{\circ}$ and dip of $60^{\circ}\pm8^{\circ}$.

The 0404 earthquake has poor focal sphere coverage because P waves of the earthquake were very emergent and could not be modeled. S wave data, with the exception of one station, were only available in a distance range of 25°-35° from ray paths that traversed the upper mantle and were difficult to model. The unconstrained moment tensor for the 0404 earthquake is only 50% double couple. This is probably not indicative of a source with a large nondouble-couple component but rather reflects the poor focal sphere coverage. The constrained and unconstrained solutions both show a smaller component of strike-slip motion than the focal mechanism obtained from first motion data.

The above inversions modeled the seismic source as a point source and made no correction for rupture propagation along a fault. This assumption is considered valid for earthquakes with a magnitude less than 6 to 6 1/4. Two of the earthquakes modeled, the 1526 and 0637:23 events, however, had magnitudes above this range. Amplitudes for these earthquakes were corrected for rupture propagation following a procedure outlined by Fitch et al. [1980].

Using rupture corrected amplitudes the unconstrained moment tensor for the 0637:23 event shows a 78% double-couple component and the southward dipping nodal plane has a strike of $88^{\circ}\pm5^{\circ}$ and dip of $50^{\circ}\pm5^{\circ}$. The corrected unconstrained moment tensor for the 1526 earthquake is 81% double couple and has a nodal plane that dips $50^{\circ}\pm5^{\circ}$ S and strikes $85^{\circ}\pm5^{\circ}$. Comparisons of these values with the solutions not corrected for rupture propagation suggest that the finiteness of the source has little influence on the solutions.

The double-couple components of the seismic moment tensors agree fairly well with the focal mechanisms of the four earthquakes, as discussed previously. Some differences in orientation may be partially explained by the frequency content of the waves used to obtain the solutions. The first motion polarities used in determining the focal mechanisms were picked from seismograms recorded on short-period instruments and gave the orientation of the fault surface during the initial part of the rupture process. These

TABLE 4b. L1 Constrained Moment Tensor Solutions

Event	Mnn*	Mne	Mee	Mnz	Mez	Mzz	Res†
0637:18	1.819	.643	.091	.157	.567	-1.910	.17
0637:23	65.8	59.9	-10.8	-11.4	50.7	-55.1	.25
1526:00	1.995	-.371	.048	-.832	.379	-2.043	.20
0404:00	2.470	-.732	-.599	-.456	1.397	-1.871	.20

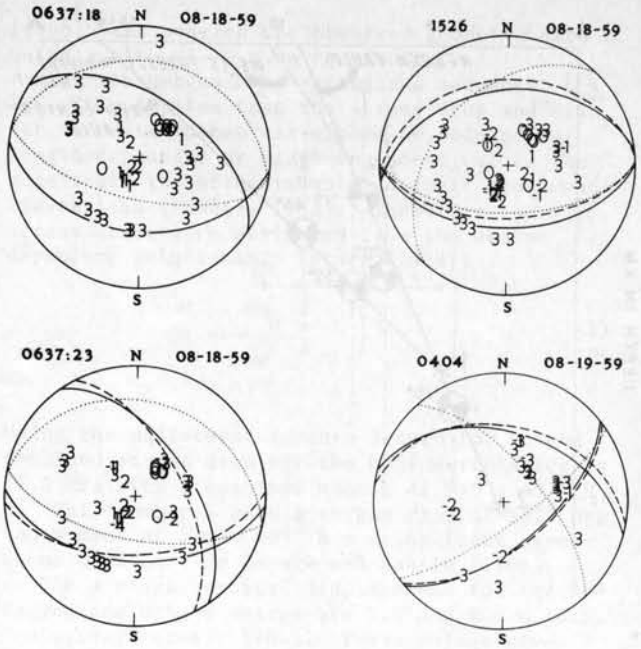

Fig. 10. Comparisons of focal mechanisms with the double-couple components of seismic moment tensors. Numbers refer to phases used in the moment tensor inversion.

first arrivals generally had periods of less than 1 s and showed only the high-frequency character of the source. Amplitude and first motion data used for the moment tensor inversions were taken from waveforms that had periods of 5-15 s. These waveforms revealed the longer-period nature of the rupture process.

Faulting Processes and Source Parameters

Short-period body wave data for the 0637:18 earthquake indicates that the earthquake initially began along a fault plane dipping $60^{\circ}\pm5^{\circ}$ to the south. Moment tensor information from long-period data suggests the rupture later propagated either upward or downward along a fault dipping $42^{\circ}\pm5^{\circ}$. Short-period data for the 0637:23 earthquake show that the rupture began on a fault dipping $60^{\circ}\pm5^{\circ}$ near the base of the seismogenic zone. The model of Sibson [1982] would suggest that the rupture probably propagated upward from this zone. Long-period data suggest that the rupture progressed along a fault dipping $50^{\circ}\pm5^{\circ}$ and that the rupture eventually broke the surface along higher-angle faults.

Two possible configurations of subsurface fault geometry that could produce the fault dips observed in the seismic and geologic data (Figure 11) are shown as idealized cross sections along the line A-A' of Figure 3. A-A' is perpendicular to the $N80^{\circ}W$ trend observed in the body wave focal mechanisms and subsidence data. At the surface the Red Canyon and Hebgen fault scarps are observed to dip $70^{\circ}\pm10^{\circ}$ and closely parallel older Laramide structures. The interpretations of Figure 11 treat the divide thrust fault as a ramplike structure, with steeply dipping faults to the south of the thrust bottoming out into this structure. The ramp dips at 46°, the mean of the dip estimates from moment tensor studies. In order to satisfy the short-period observations, both subevents of the main shock (1 and 2) begin along a fault that dips 60° to the south. The subevents in Figure 11 are not plotted at the epicenter locations shown in Figure 5 but are plotted where fault plane solutions, moment tensors, and waveform modeling results suggest that they may have occurred with respect to the observed surface breakage. Although both interpretations depict the first subevent as occurring along the same fault plane as the second subevent, the accuracy of the hypocenter locations is not sufficient to determine whether or not this assumption is valid.

Figure 11 (left) suggests a steeply dipping fault that may merge into the ramp fault south of the Hebgen fault. There is no seismic information available to determine whether or not the ramp fault continues south of the fault juncture, and if it does continue, whether or not it begins to flatten. The steeply dipping fault on which the two events occurred could represent a normal fault that joins a shallower Laramide fault updip of the hypocenters. The rupture followed this fault system until reaching the Hebgen and Red Canyon faults, where it propagated upward to the surface.

Another interpretation is offered in Figure 11 (right). In this diagram the Hebgen fault cuts through an older thrust fault, and the two earthquakes could have occurred along the lower part of the Hebgen fault. As the 0637:23 event ruptured upward along the Hebgen fault, it reactivated the thrust fault and propagated upward to break the surface at the Red Canyon fault.

Composite fault plane solutions obtained from microearthquakes in the region by Smith et al. [1977] and Trimble and Smith [1975] are not sufficient to reject either hypothesis. North of the subsurface projection of the Hebgen fault, two composite fault plane solutions have nodal planes that dip southward $46^{\circ}\pm5^{\circ}$ and $52^{\circ}\pm5^{\circ}$. This coincides with the projection of the ramp fault that dips 46°. South of these solutions, Trimble and Smith [1975] obtained two composite solutions with nodal planes that dip $70^{\circ}\pm5^{\circ}$ S. These correlate well with the projected dip of the Hebgen fault based on a $70^{\circ}\pm10^{\circ}$ dip at the surface. Another composite solution with a nodal plane dipping $70^{\circ}\pm5^{\circ}$ S is located in the region where the two earthquakes occurred and agrees well with the $60^{\circ}\pm5^{\circ}$ dip obtained from short-period first motion data.

Although the Hebgen and Red Canyon faults had comparable maximum vertical displacements, average displacement along the Red Canyon fault was about twice that along the Hebgan fault [U.S. Geological Survey, 1964]. If this relationship holds at depth, then a model that treats the Red

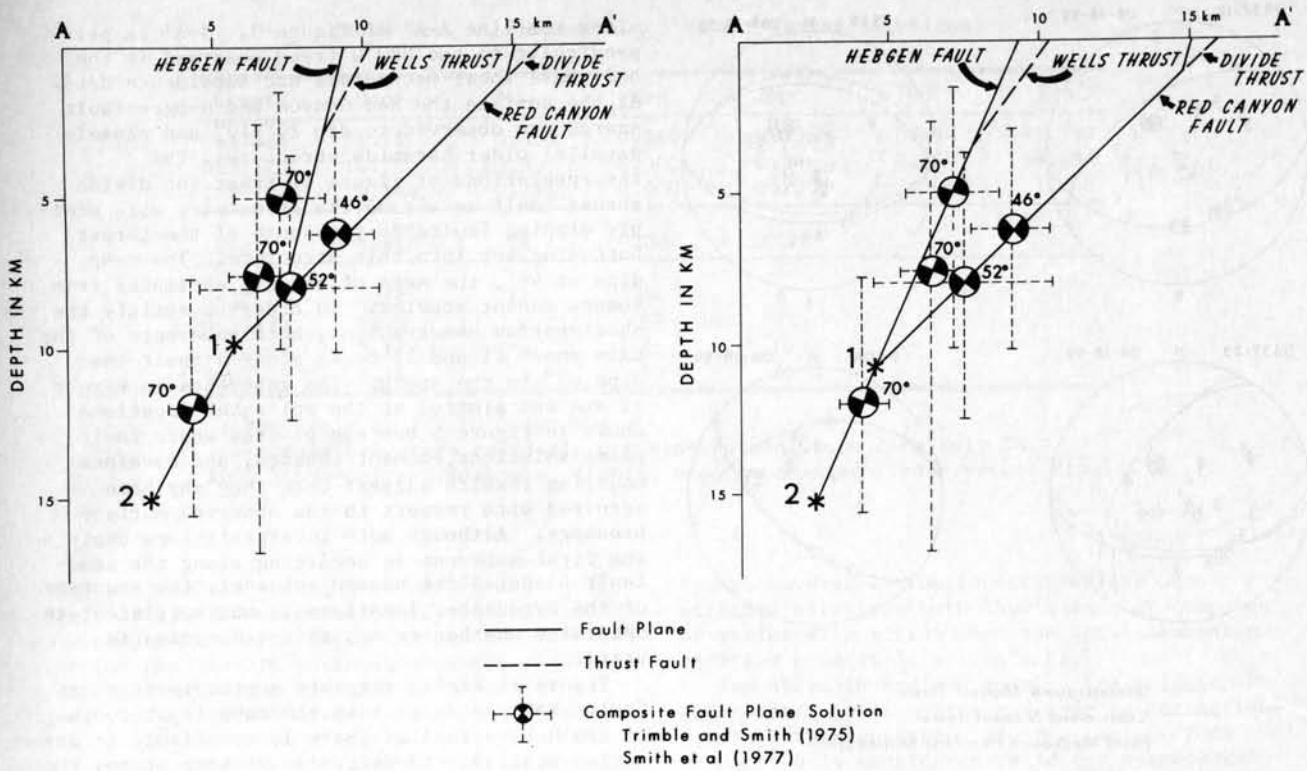

Fig. 11. Idealized cross sections of the geometry of the Hebgen-Red Canyon fault system. Alternative interpretations are shown in the left side and the right side. The hypocenters of the 0637 earthquake, denoted by asterisks, are plotted where fault plane solution, moment tensor, and waveform modeling results suggest that they may be located with respect to the surface faulting. Cross sections are along the line A-A' shown in Figure 3. Side views of composite fault plane solutions from Smith et al. [1977] and Trimble and Smith [1975] are also shown.

Canyon fault as the major structure controlling the faulting process (Figure 11 (left)) would be favored.

It is important to note that the interpretations of Figure 11 are by no means unique. Other fault configurations may exist that fit the seismic and geologic data equally well. For example, in order to produce an average dip of 46°, as seen in the analysis of long-period out long period radiation from the high-angle fault segments. On the other hand, if the average displacement along the high-angle fault segments was considerably smaller than the displacement along the low-angle segments, significant long-period energy may not have been radiated by the steeply dipping segments.

Additional source parameters were obtained for the four earthquakes using information from the moment tensor solutions and waveform modeling. If we consider a unilateral rupture model where L is the fault length, W the fault width, D the dislocation, and v the rupture velocity, then the approximate fault length can be estimated from $t_c \sim L/v$, where t_c is the rupture time from Table 3 (the rise time plus the plateau time). A 3 km/s rupture velocity was used [Kanamori and Stewart, 1976]. Source parameters are listed in Table 3. If bilateral propagation along the strike of the fault plane is assumed, the fault length is twice the unilateral fault length.

For a unilateral propagating fault, the fault length estimates for the 0637:18 and 0637:23 earthquakes are 6 and 21 km. These values agree well with the 30-km length estimated by modeling of geodetic data [Savage and Hastie, 1966] and with the surface fault lengths of 14.5 km (Hebgen fault) and 23 km (Red Canyon fault) measured by the U.S. Geological Survey [1964]. This observation and the fact that all relocations of the subevents placed the epicenters near the southeastern end of the surface faulting suggests unilateral rupture in a northwestward direction. When we combine this information with the earlier observation that the second subevent occurred at or near the base of the seismogenic zone, it appears that rupture during this subevent propagated both updip and along strike. This is similar to the rupture process observed in the 1983 Borah Peak, Idaho earthquake [Doser and Smith, 1985].

The dislocation D is given by $D = M_o / \mu w L$, where M_o is the seismic moment, μ is the shear modulus, and w is the fault width. A shear modulus of 3.3×10^{11} dyn/cm^2 was assumed. The widths are estimated from the focal depths and the dips of the nodal planes of the double-couple components of the seismic moment tensors. Using the unilateral rupture length for L, the average displacement for the 0637:18 earthquake is 0.95 m and for the 0637:23 earthquake is 6.8 m. A maximum subsidence of 7 m was measured in the West Yellowstone basin after the earthquakes, and Savage and Hastie

[1966] best modeled the observed geodetic data using a slip of 10 m on the fault.

For the Hebgen Lake earthquake sequence, $L \leq 2W$. This implies that the stress drop and slip for the earthquakes can either be modeled as length-dependent or width-dependent, since the models are indistinguishable in their gross manifestations [Scholz, 1982]. Therefore the stress drops were estimated from the width-dependent relationship [Starr, 1928]:

$$\Delta\sigma = \frac{8M_o}{3\pi W^2 L} \quad (1)$$

Using the unilateral rupture length for L, the combined stress drop for the 0637 earthquakes is 11.5 MPa with a combined moment of 9.5×10^{19} N m. This compares with a stress drop of 18.7 MPa and moment of 1.5×10^{20} N m using fault dimensions derived from Savage and Hastie [1966].

The average vertical displacement for the Red Canyon and Hebgen scarps are 2.4 and 1.6 m [U.S. Geological Survey, 1964]. These values give stress drop estimates of 4.2 and 2.7 MPa, and moments of 2.9×10^{19} and 1.2×10^{19} Nm, using a 70^{o} dip and 15 km depth. Although these stress drop and moment values are 40-60% lower than the seismologically determined values, they are within the limits of error associated with these estimates. This supports the idea that the 0637 earthquakes produced the observed surface rupture and that epicenters located north and east of the fault scarps are mislocated by 5 or 10 km.

Conclusions

The study of the seismograms of the 1959 (M_S = 7.5) Hebgen Lake main shock and its aftershocks has revealed important information about a large normal fault earthquake sequence in the intermountain region. Geodetic, geologic, and seismic information suggests that the two subevents of the main shock on August 18, 1959, at 0637 UT may represent normal faulting along reactivated Laramide thrusts. Focal mechanisms for aftershocks of the 1959 Hebgen Lake sequence and other earthquakes in the northwestern Yellowstone region reveal a complex pattern of faulting. Preexisting faults that are favorably oriented to the present day stress field as well as younger Quaternary faults appear to be seismically active, producing localized perturbations in the stress field that make it difficult to determine generalized regional stress orientations. The region is undergoing north-south extension as far east as the Mammoth fault, although Quaternary normal faults in the region strike north and northwest. The Norris Junction area near the caldera boundary is undergoing northeast-southwest extension; however, 10 km to the north an aftershock of the 1959 Hebgen Lake sequence shows northwest-southeast extension. This suggests a rapidly varying stress field near the caldera boundary. Other aftershocks of the 1959 sequence exhibit strike-slip and reverse fault mechanisms that may be reflective of local variations in stress.

Focal depth data for $M \geq 4.5$ earthquakes in the Hebgen Lake-northwestern Yellowstone region suggest that the depth to the base of the seismogenic zone decreases from 15 to 17 km in the Hebgen Lake region to 6 km or less as one moves eastward toward the Yellowstone caldera boundary. Similar changes in maximum focal depth were seen in previous studies of microseismicity [Smith et al., 1977]. Observed depths to the base of the seismogenic zone eastward across the region agree well with depths to the brittle-ductile transition zone estimated from observed heat flow values and the models of Smith and Bruhn [1984].

Acknowledgments. I would like to thank W. J. Arabasz, R. L. Bruhn, T. J. Owens, J. C. Pechmann, R. B. Smith, and G. Zandt for their helpful suggestions and comments. Seismograms for this study were generously provided by R. A. Uhrhammer and B. A. Bolt. G. E. Randall provided needed advice on processing the digital data. This work was supported by a University of Utah Graduate Research Fellowship. Computer time for the analysis was provided by the University of Utah Seismograph Stations. Drafting costs were paid by the University of Utah Geophysics Special Funds.

References

Arabasz, W. J., and R. B. Smith, Introduction: What you've always wanted to know about earthquakes in Utah, in Earthquake Studies in Utah 1850 to 1978, edited by W. J. Arabasz, R. B. Smith and W. D. Richins, pp. 1-14, University of Utah Seismograph Stations, 1979.

Arabasz, W. J., W. D. Richins, and C. J. Langer, The Pocatello Valley (Utah-Idaho border) earthquake sequence of March to April 1975, Bull. Seismol. Soc. Am., 71, 803-826, 1981.

Armstrong, R. L., W. B. Leeman, and H. E. Maulde, K-Ar dating, Quaternary and Neogene volcanic rocks of the Snake River Plain, Idaho, Am. J. Sci., 275, 225-251, 1975.

Bache, T. C., D. G. Lambert, and T. G. Barker, A source model for the March 28, 1975, Pocatello Valley earthquake from time-domain modeling of teleseismic P-waves, Bull. Seismol. Soc. Am., 70, 405-418, 1980.

Bullen, K. E., An Introduction to the Theory of Seismology, Cambridge Press, New York, 1963.

Claerbout, J. F., and F. Muir, Robust modeling with erratic data, Geophysics, 83, 826-844, 1973.

Dewey, J. W., W. H. Dillinger, J. Taggart, and S. T. Algermissen, A technique for seismic zoning: Analysis of earthquake locations and mechanisms in northern Utah, Wyoming, Idaho and Montana, NOAA Tech. Rep., ERL267-ESL30, 28-48, 1973.

Doser, D. I., The 1959 Hebgen Lake, MT and the 1983 Borah Peak, ID earthquakes: Examples of large normal fault events in the Intermountain region (abstract), Earthquake Notes, 55, 14, 1984a.

Doser, D. I., The 1983 Borah Peak, Idaho and

1959 Hebgen Lake, Montana earthquakes: Models for normal fault earthquakes in the Intermountain seismic belt, paper presented at the U.S. Geological Survey Sun Valley Conference on the Borah Peak Earthquake, Sun Valley, Idaho, 1984b.

Doser, D. I., and R. B. Smith, Seismicity of the Teton-southern Yellowstone region, Wyoming, Bull. Seismol. Soc. Am., 73, 1369-1394, 1983.

Doser, D. I., and R. B. Smith, Source parameters of the October 1983 Borah Peak, Idaho earthquake from body wave analysis, Bull. Seismol. Soc. Am., in press, 1985.

Ewing, M., W. Jardetzky, and F. Press, Elastic Waves in Layered Media, McGraw-Hill, New York, 1957.

Fitch, T. J., D. W. McCowan, and M. W. Shields, Estimation of the seismic moment tensor from teleseismic body wave data with applications to intraplate and mantle earthquakes, J. Geophys. Res., 85, 3817-3828, 1980. (Correction and addition to, J. Geophys. Res., 86, 9375-9376, 1981.)

Furlong, K. P., An analytic stress model applied to the Snake River Plain (northern Basin and Range province, U.S.A.), Tectonophysics, 58, T11-T15, 1979.

Herrin, E. (Chairman), Seismological table for P phases, Bull. Seismol. Soc. Am., 58, 1193-1351, 1968.

Jeffreys, H., and K. E. Bullen, Seismological Tables, British Association for the Advancement of Science, London, 1940.

Kanamori, H., and G. S. Stewart, Mode of strain release along the Gibbs fracture zone, Mid-Atlantic Ridge, Phys. Earth Planet. Inter., 11, 312-332, 1976.

Mathieson, E. L., Post-Pinedale displacement rate on the Madison Range fault along its 1959 rupture trace, Madison County, Montana (abstract), Geol. Soc. Am. Abstr. Program, 15, 376, 1983.

Myers, W. F., and W. Hamilton, Deformation accompanying the Hebgen Lake earthquake of August 17, 1959, U.S. Geol. Surv. Prof. Pap., 435, 37-98, 1964.

Pfiffner, O. A., and J. G. Ramsay, Constraint on geologic strain rates: Arguments from finite strain rates of naturally deformed rocks, J. Geophys. Res., 87, 311-321, 1982.

Pitt, A. M., C. S. Weaver, and W. Spence, The Yellowstone Park earthquake of June 30, 1975, Bull. Seismol. Soc. Am., 69, 187-205, 1979.

Qamar, A. I., and M. C. Stickney, Montana earthquakes, 1869-1979, Historical seismicity and earthquake hazard, Mem. Mont. Bur. Mines Geol., 51, 1-53, 1983.

Reilinger, R. E., G. P. Citron, and L. D. Brown, Recent vertical crustal movements from precise leveling data in southwestern Montana, western Yellowstone National Park, and the Snake River Plain, J. Geophys. Res., 82, 5349-5359, 1977.

Ryall, A., The Hebgen Lake Montana, earthquake of August 17, 1959, P-waves, Bull. Seismol. Soc. Am., 52, 235-271, 1962.

Savage, J. C., and L. M. Hastie, Surface deformation associated with dip-slip faulting, J. Geophys. Res., 71, 4897-4904, 1966.

Scholz, C. H., Scaling laws for large earthquakes: Consequences for physical models, Bull. Seismol. Soc.Am., 72, 1-14, 1982.

Sengupta, M. K., The structure of the earth's mantle from body wave observations, Ph.D. thesis, Mass. Inst. of Technol., Cambridge, 1975.

Sibson, R. H., Fault zone models, heat flow, and the depth distribution of earthquakes in the continental crust of the United States, Bull. Seismol. Soc. Am., 72, 151-164, 1982.

Smith, R. B., and R. L. Bruhn, Intraplate extensional tectonics of the western U.S. Cordillera: Inferences on structural style from seismic reflection data, regional tectonics and thermal-mechanical models of brittle/ductile deformation, J. Geophys. Res., 89, 5733-5762, 1984.

Smith, R. B., and R. L. Christiansen, Yellowstone Park as a window on the earth's interior, Sci. Am., 242, 104-117, 1980.

Smith, R. B., and M. L. Sbar, Contemporary tectonics and seismicity of the western United States with emphasis on the Intermountain seismic belt, Geol. Soc. Am. Bull., 85, 1205-1218, 1974.

Smith, R. B., R. T. Shuey, J. R. Pelton, and J. P. Bailey, Yellowstone hot spot: Contemporary tectonics and crustal properties from earthquake and aeromagnetic data, J. Geophys. Res., 82, 3665-3676, 1977.

Smith, R. B., M. M. Schilly, L. W. Braile, J. Ansorge, J. L. Lehman, M. R. Baker, C. Prodehl, J. H. Healy, S. Mueller, and R. W. Greensfelder, The 1978 Yellowstone-eastern Snake River Plain seismic profiling experiment: Crustal structure of the Yellowstone region and experiment design, J. Geophys. Res., 87, 2583-2596, 1982.

Starr, A. T., Slip in a crystal and rupture in a solid due to shear, Proc. Cambridge Philos. Soc., 24, 489-500, 1928.

Strelitz, R. A., Moment tensor inversions and source models, Geophys. J. R. Astron. Soc., 52, 359-364, 1978.

Trimble, A. B., Seismicity and contemporary tectonics of the Yellowstone Park-Hebgen Lake region, M.S. thesis, Univ. of Utah, Salt Lake City, 1973.

Trimble, A. B., and R. B. Smith, Seismicity and contemporary tectonics of the Hebgen Lake-Yellowstone Park region, J. Geophys. Res., 80, 733-741, 1975.

U.S. Geological Survey, The Hebgen Lake, Montana, earthquake of August 17, 1959, U.S. Geol. Surv. Prof. Pap., 435, plates 2 and 5, 1964.

U.S. Geological Survey, Geologic map of Yellowstone National Park, U.S. Geol. Surv. Misc. Geol. Invest. Map I-711, 1972.

Vetter, U. R., and A. S. Ryall, Systematic change of focal mechanism with depth in the western Great Basin, J. Geophys. Res., 88, 8237-8250, 1983.

Witkind, I. J., Reactivated faults north of

Hebgen Lake, U.S. Geol. Surv. Prof. Pap., 435, 37-50, 1964.

Witkind, I. J., J. B. Hadley, and W. H. Nelson, Pre-Tertiary stratigraphy and structure of the Hebgen Lake area, U.S. Geol. Surv. Prof. Pap., 435, 199-208, 1964.

D. I. Doser, Seismological Laboratory, California Institute of Technology, MS/252-21, Pasadena, CA 91125.

(Received June 21, 1984;
revised January 4, 1985;
accepted January 24, 1985)